

RESEARCH ARTICLE | SEPTEMBER 09 2024

## GdWN<sub>3</sub> is a nitride perovskite






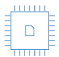
Rebecca W. Smaha ; John S. Mangum ; Neha Yadav ; Christopher L. Rom ; Brian M. Wieliczka ; Baptiste Julien ; Andrew Treglia ; Craig L. Perkins ; Prashun Gorai ; Sage R. Bauers ; Andriy Zakutayev 



*Appl. Phys. Lett.* 125, 112902 (2024)


<https://doi.org/10.1063/5.0219503>



 Nanotechnology & Materials Science  Optics & Photonics  Impedance Analysis  Scanning Probe Microscopy  Sensors  Failure Analysis & Semiconductors

Unlock the Full Spectrum.  
From DC to 8.5 GHz.  
Your Application. Measured.

[Find out more](#)



# GdWN<sub>3</sub> is a nitride perovskite

Cite as: Appl. Phys. Lett. **125**, 112902 (2024); doi: [10.1063/5.0219503](https://doi.org/10.1063/5.0219503)

Submitted: 17 May 2024 · Accepted: 23 August 2024 ·

Published Online: 9 September 2024



View Online



Export Citation



CrossMark

Rebecca W. Smaha,<sup>1,a)</sup> John S. Mangum,<sup>1</sup> Neha Yadav,<sup>2</sup> Christopher L. Rom,<sup>1</sup> Brian M. Wieliczka,<sup>1</sup> Baptiste Julien,<sup>1</sup> Andrew Treglia,<sup>3</sup> Craig L. Perkins,<sup>1</sup> Prashun Gorai,<sup>1,2,4</sup> Sage R. Bauers,<sup>1</sup> and Andriy Zakutayev<sup>1,a)</sup>

## AFFILIATIONS

<sup>1</sup>National Renewable Energy Laboratory, Golden, Colorado 80401, USA

<sup>2</sup>Colorado School of Mines, Golden, Colorado 80401, USA

<sup>3</sup>Colorado State University, Fort Collins, Colorado 80521, USA

<sup>4</sup>Rensselaer Polytechnic Institute, Troy, New York 12180, USA

<sup>a)</sup>Authors to whom correspondence should be addressed: [Rebecca.Smaha@NREL.gov](mailto:Rebecca.Smaha@NREL.gov) and [Andriy.Zakutayev@NREL.gov](mailto:Andriy.Zakutayev@NREL.gov)

## ABSTRACT

Nitride perovskites  $ABN_3$  are an emerging and highly underexplored class of materials that are of interest due to their intriguing calculated ferroelectric, optoelectronic, and other functional properties. Incorporating novel  $A$ -site cations is one strategy to tune and expand such properties; for example,  $Gd^{3+}$  is compelling due to its large magnetic moment, potentially leading to multiferroic behavior. However, the theoretically predicted ground state of  $GdWN_3$  was a non-perovskite monoclinic structure. Here, we experimentally show that  $GdWN_{3-y}$  crystallizes in a perovskite structure. High-throughput combinatorial sputtering with activated nitrogen is employed to synthesize thin films of  $Gd_{2-x}W_xN_{3-y}O_y$  with oxygen content  $y < 0.05$ . *Ex situ* annealing crystallizes a polycrystalline perovskite phase in a narrow composition window near  $x = 1$ . LeBail fits of synchrotron grazing incidence wide angle x-ray scattering data are consistent with a perovskite ground-state structure. Refined density functional theory calculations that included antiferromagnetic configurations confirm that the ground-state structure of  $GdWN_3$  is a distorted  $Pnma$  perovskite with antiferromagnetic ordering, in contrast to prior predictions. Initial property measurements find that  $GdWN_{3-y}$  is paramagnetic down to  $T = 2$  K with antiferromagnetic correlations and that the absorption onset depends on cation stoichiometry. This work provides an important path toward both the rapid expansion of the emerging family of nitride perovskites and understanding their potential multiferroic properties.

© 2024 Author(s). All article content, except where otherwise noted, is licensed under a Creative Commons Attribution (CC BY) license (<https://creativecommons.org/licenses/by/4.0/>). <https://doi.org/10.1063/5.0219503>

Nitride perovskites  $ABN_3$  are currently of high interest due to the exciting piezoelectricity observed for  $LaWN_3$ .<sup>1</sup> Only five nitride perovskites have been reported experimentally:  $TaThN_3$ ,<sup>2</sup>  $LaWN_3$ ,<sup>1,3</sup>  $LaReN_3$ ,<sup>4</sup>  $CeWN_3$ , and  $CeMoN_3$ .<sup>5</sup> However, theoretical calculations have predicted that a wide phase space of nitride perovskites should exist with highly oxidized  $B$  cations such as  $W^{6+}$ ,  $Re^{6+/7+}$ ,  $Mo^{6+}$ ,  $Ta^{5+}$ ,  $Nb^{5+}$ ,  $Cr^{6+}$ , or  $Os^{6+/8+}$ .<sup>5–10</sup> While they are predicted to be stable, in practice, it is challenging to synthesize these materials. However, many oxynitride perovskites [i.e.,  $ABO_xN_{3-x}$ , where  $x$  is at least 0.5 (Ref. 11)] and nitrogen-poor antiperovskite nitrides (i.e.,  $M_3NE^{12}$ ) have been reported compared to only five nitride perovskites, demonstrating that synthesizing nitride-rich materials is a greater challenge.

The challenges of controlling composition and impurities in synthesizing nitride perovskites include the possibilities of oxygen incorporation, nitrogen deficiency, and slight cation off-stoichiometry. Indeed, the oxygen content of the first reported nitride perovskite,

$TaThN_3$ ,<sup>2</sup> was not studied, and nitrogen deficiency was observed in  $LaWN_3$ .<sup>1,13</sup> The most successful techniques toward stoichiometric nitride perovskites have been radio frequency sputtering,<sup>1,5</sup> which increases the chemical potential of nitrogen and is a highly energetic process, and high-pressure high-temperature methods.<sup>3,4</sup> In addition to phase stability, calculations predicted that several rare-earth nitride perovskites should exhibit ferroelectric behavior and be semiconducting.<sup>6</sup>  $LaWN_3$  was shown to have a large piezoelectric response and thus polar symmetry.<sup>1</sup> However, its properties are highly sensitive to stoichiometry, necessitating precise synthetic control in order to functionalize this material—as is the case for many semiconductors.<sup>14</sup>

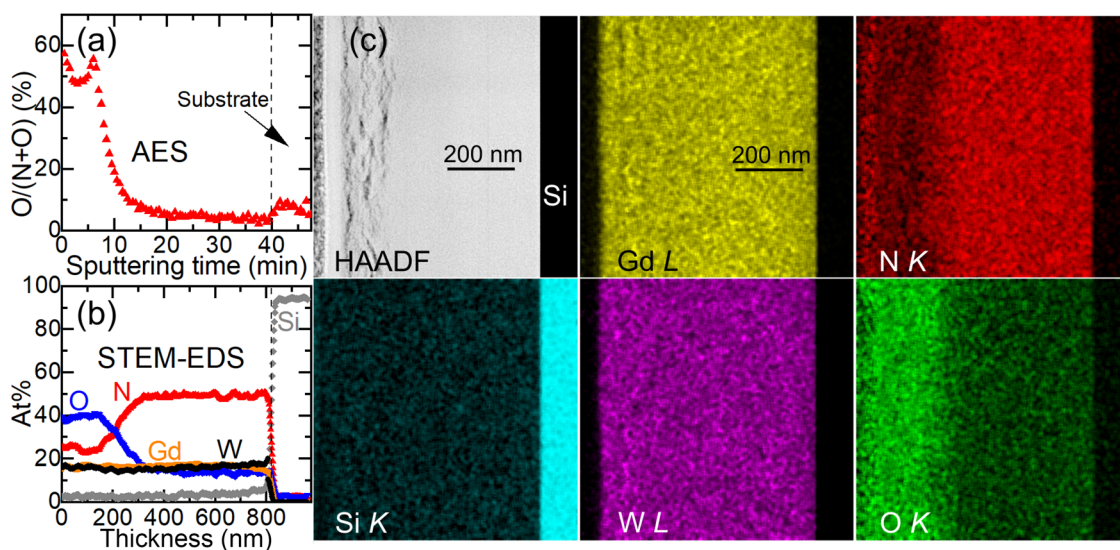
Expanding the palette of  $A$  cations can broaden the functionalities of nitride perovskites. One attractive target is multiferroicity, in which a material exhibits ferroelectric and magnetic order simultaneously. Multiferroics are emerging options for electronic applications such as low-power field sensing, memory recording/storage technologies, and

spintronic devices.<sup>15,16</sup> However, achieving both ferroic orders simultaneously is difficult: ferroelectricity normally arises from an ionic displacement that breaks inversion symmetry, but this is generally related to a  $d^0$  electronic structure or a lone pair, precluding magnetic order in transition metals such as Fe and Mn.<sup>16</sup> Thus,  $A = \text{Gd}^{3+}$  is an attractive option, as  $\text{Gd}^{3+}$  has one of the largest magnetic moments ( $8 \mu_B$ ), and elemental Gd is unique among the rare earths in being ferromagnetic (FM) at room temperature. Recent calculations examined the ground-state structure of  $\text{GdWN}_3$  but did not consider the possible antiferromagnetic (AFM) ordering of  $\text{Gd}^{3+}$ , which is crucial for the correct identification of the ground-state structure. These calculations yielded a non-perovskite monoclinic ( $C2/c$ ) ground-state structure.<sup>8,17</sup> However, additional magnetic structure calculations of two perovskite phases that were slightly higher-energy than the ground state indicated large ferroelectric polarization and AFM order (albeit with Néel temperature  $T_N < 8$  K), raising the possibility of stabilizing a single-phase multiferroic.<sup>17</sup>

Here, we conclusively show that  $\text{Gd}_{2-x}\text{W}_x\text{N}_{3-y}\text{O}_y$ , with  $x \approx 1$  and oxygen content  $y \leq 0.05$ , subsequently referred to as  $\text{GdWN}_{3-y}$ , can be experimentally realized as a perovskite using high-throughput synthesis and characterization. We employ combinatorial sputtering with activated nitrogen to survey the  $\text{Gd}_{2-x}\text{W}_x\text{N}_{3-y}$  phase space and use a variety of microscopy and x-ray techniques to probe its composition and crystal structure. Strikingly, a perovskite phase crystallizes close to the  $\text{GdWN}_{3-y}$  composition. Confirming the experimental results, we use first-principles calculations to show that a perovskite phase ( $Pnma$ ) with AFM ordering is the ground-state structure of  $\text{GdWN}_3$ . We perform initial property measurements, finding that  $\text{GdWN}_{3-y}$  is paramagnetic (PM) down to  $T = 2$  K, in contrast to previous computational predictions. We also find a large change in optical absorption across the  $\text{Gd}_{2-x}\text{W}_x\text{N}_{3-y}$  gradient. This work yields improved understanding of the thermodynamics within—and significantly expands—the small phase space of experimentally reported nitride perovskites.

Combinatorial deposition of  $\text{Gd}_{2-x}\text{W}_x\text{N}_{3-y}$  was performed with RF co-sputtering onto Si and sapphire substrates held at high temperature ( $\sim 700^\circ\text{C}$ ), yielding compositionally graded films with a cation gradient roughly  $35\% < \text{Gd}/(\text{W} + \text{Gd}) < 65\%$  (i.e.,  $\text{Gd}_{0.7}\text{W}_{1.3}\text{N}_{3-y}$  to  $\text{Gd}_{1.3}\text{W}_{0.7}\text{N}_{3-y}$ ). Cation composition  $\text{Gd}/(\text{W} + \text{Gd})$  was mapped across the combinatorial films using x-ray fluorescence (XRF), and select points were measured with Auger electron spectroscopy (AES) sputter depth profiling and scanning transmission electron microscopy energy-dispersive x-ray spectroscopy (STEM-EDS) to probe the anion stoichiometry. As W and Si have overlapping lines in XRF, STEM-EDS, and AES, films on sapphire substrates were used to calibrate the composition.

AES depth profiling [Fig. 1(a)] shows an oxygenated surface layer, potentially implying the presence of some amorphous Gd oxide ( $\text{GdO}_x$ ). However, it also indicates O content in most of the film closer to  $\sim 5\% \text{ O}/(\text{N} + \text{O})$ , which is typical for sputtered nitrides.<sup>18–20</sup> STEM-EDS elemental mapping performed on this sample [Figs. 1(b) and 1(c)] exhibit no obvious segregation of Gd and W throughout the film, but there are clear signs of oxidation near the surface due to air exposure post-deposition. A line profile extracted from STEM-EDS [Fig. 1(b)] exhibits roughly equal cation stoichiometry [i.e.,  $\text{Gd}/(\text{W} + \text{Gd}) \approx 50\%$ ] and shows the lamella oxidized easily. STEM-high-angle annular dark-field (HAADF) imaging associated with the STEM-EDS maps and 4D-STEM reveal a large amorphous region near the surface, consistent with the AES and STEM-EDS results and likely due to post-deposition oxidation [Fig. 1(c) and Fig. S1]. 4D-STEM (Fig. S1) shows that the grain size ranges from approximately 130–200 nm. Additionally, a few laterally aligned voids that may be delamination induced by an *ex situ* rapid thermal annealing step are visible in Fig. 1(c). A scanning electron microscopy image of an annealed combinatorial film is shown in Fig. S2 and exhibits similar laterally aligned voids near the top surface of the film. AES profiling performed on a freshly deposited sample (Fig. S3) exhibits similar O



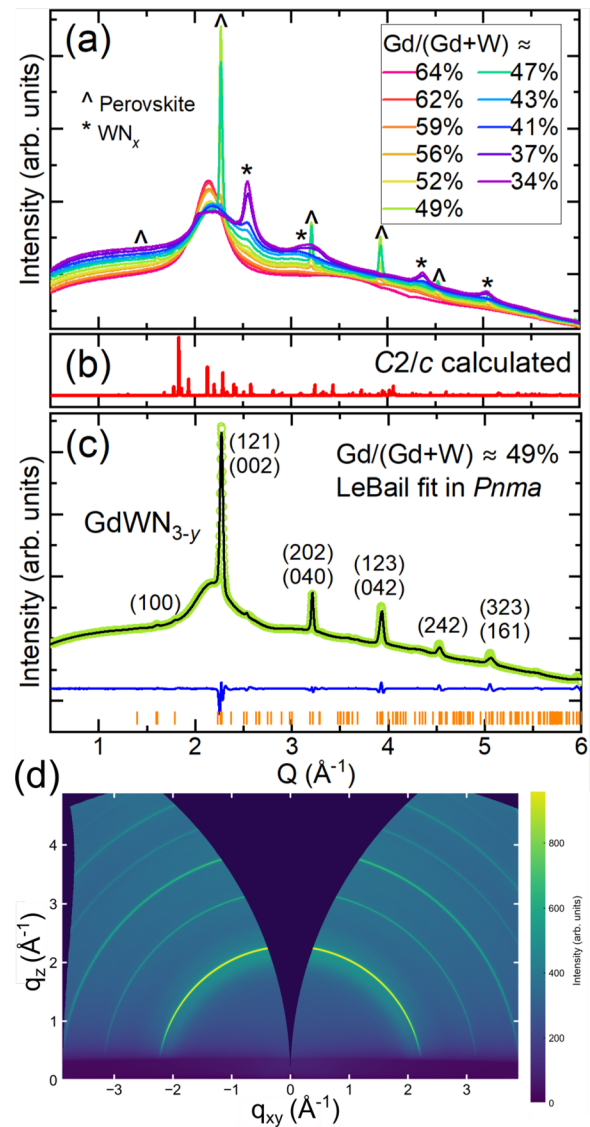
**FIG. 1.** (a) Cation ratio  $\text{O}/(\text{N} + \text{O})$  extracted from the AES sputter depth profile of this sample. (b) STEM-EDS at. % line profile through the film. (c) STEM-EDS elemental mapping at the Gd L-peak, W L-peak, N K-peak, and O K-peak and associated HAADF image. Due to overlapping W/Si EDS lines, in (c), it erroneously appears the film contains some Si; in (b), the Si signal has been added to W through the film. All measurements were performed on a region of an annealed combinatorial film with  $\text{Gd}/(\text{W} + \text{Gd}) \approx 47\%$ .

content in the bulk (2%–4%) and a thinner region of higher O near the surface, confirming that the O seen in the sample analyzed with AES/STEM (Fig. 1) is from post-growth oxidation, potentially including from the *ex situ* annealing step and/or oxidation of the lamella.

*Ex situ* rapid thermal annealing in flowing  $N_2$  causes the as-deposited amorphous/nanocrystalline films to crystallize near the  $GdWN_3$  composition. Laboratory x-ray diffraction data of an as-deposited film and the same film annealed at  $950^\circ C$  are in Fig. S4. Synchrotron grazing incidence wide angle x-ray scattering (GIWAXS) was employed to study the structure of this annealed film along the composition gradient [Fig. 2(a)]. The combinatorial GIWAXS data show that the width of the new phase in composition space is narrow, less than 10%  $Gd/(W + Gd)$ , and the highest crystallinity is found near stoichiometric  $GdWN_{3-y}$ . In addition to this new phase, a broad amorphous peak at  $Q \approx 2.1 \text{ \AA}^{-1}$  is often observed on the Gd-rich side of the films after annealing, likely arising from a  $GdO_x$  impurity. On the W-rich side of the films, broad peaks arising from  $WN_x$  are visible. In some films, metallic W and/or  $GdO_x$  crystallized on the W- and Gd-rich sides of the film, respectively (Figs. S4 and S6).

Comparing the peaks of the unidentified crystalline phase to the simulated pattern of the previously calculated monoclinic  $C2/c$  ground-state structure [Fig. 2(b)] does not yield a match. Instead, the pattern is well-matched by a perovskite phase, as shown with carets in Fig. 2(a). A GIWAXS 2D detector image [Fig. 2(d)] indicates that this perovskite phase is polycrystalline. To confirm the unexpected discovery of a perovskite structure, we performed LeBail fits on GIWAXS data of a film region with  $Gd/(W + Gd) \approx 49\%$  in three possible perovskite space groups ( $Pm\bar{3}m$ ,  $R3c$ , and  $Pnma$ ). The LeBail method was chosen as full Rietveld refinements on thin-film XRD data can be complex and less trustworthy due to texturing and orientation effects. Orthorhombic  $Pnma$  yields the best fit [Fig. 2(c)]; fits to polar  $R3c$  (in which  $LaWN_{3-y}$  crystallizes<sup>1,3,14</sup>) and the prototypical cubic perovskite  $Pm\bar{3}m$  are statistically equivalent to each other (Fig. S5). A summary of the extracted lattice parameters and fit metrics is in Table I. We note that the annealing temperature required to crystallize the  $GdWN_{3-y}$  perovskite phase is  $900\text{--}950^\circ C$ , slightly higher than that required to crystallize  $LaWN_{3-y}$  ( $\sim 800^\circ C$ ),<sup>1,14</sup> and that the narrow phase width is consistent with previous results seen for  $LaWN_{3-y}$ .<sup>14</sup>

As our experimental results are inconsistent with previous computational predictions of the structure of  $GdWN_3$ , we performed additional density functional theory calculations to search for the magnetic ground-state structure of  $GdWN_3$ . We considered six polymorphic structures (both perovskite and non-perovskite phases) in the following space groups: perovskites  $Pm\bar{3}m$ ,  $Pnma$ ,  $P4mm$ ,  $R3c$ , and  $R\bar{3}c$ , and non-perovskite  $C2/c$  (previously calculated as the ground state<sup>8,17</sup>); see the supplementary material for details. Considering only FM ordering, the ground-state energy of the perovskite  $Pnma$  and the non-perovskite  $C2/c$  phases are similar (Table S1), which agrees with prior computational work that found monoclinic  $C2/c$  to be the ground-state structure.<sup>8,17</sup> Next, we considered various AFM configurations of  $Gd^{3+}$  to search for magnetic orderings that are lower energy than FM, as the huge magnetic moment of  $Gd^{3+}$  must play an important role in phase stability. Interestingly, we find a distorted perovskite phase in orthorhombic  $Pnma$  [Figs. 3(b) and 3(c)] to be a lower-energy structure for  $GdWN_3$ . The relative energies of the polymorphic structures in their lowest-energy magnetic ordering are shown in Fig. 3(a) and Table S1, and the relaxed structures are shown in Fig. S8. Cubic



**FIG. 2.** (a) Synchrotron grazing incidence wide angle x-ray scattering (GIWAXS) data along a compositionally graded  $GdWN_{3-y}$  film. (b) Simulated pattern of the previously calculated monoclinic  $C2/c$  ground-state structure. (c) LeBail fit of the synchrotron GIWAXS dataset with  $Gd/(W+Gd) \approx 49\%$  in  $Pnma$  perovskite symmetry. The data (green circles), fit (black line), and residual (blue line) are shown. (d) GIWAXS 2D detector image of the film shown in (c).

perovskite  $Pm\bar{3}m$  has the highest energy in comparison to the other phases, implying that symmetry-lowering, including octahedral distortions and tilting, stabilizes the other perovskite phases ( $Pnma$ ,  $P4mm$ ,  $R3c$ ,  $R\bar{3}c$ ). The calculated and experimental lattice parameters extracted from LeBail fits of three of the possible space groups are in close agreement, with the best agreement for the  $Pnma$  phase, further indicating that this phase is the ground-state structure (Table I). While these data and refinements confirm that  $GdWN_{3-y}$  crystallizes within the perovskite family, future work will be needed to definitively assign the symmetry.

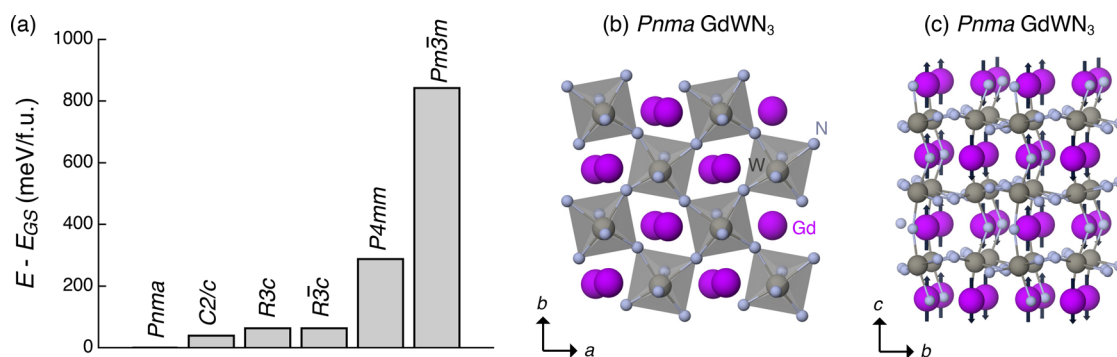
**TABLE I.** Comparison of calculated lattice parameters to lattice parameters extracted from LeBail refinements of GIWAXS data [see Fig. 2(c) and Fig. S5], and the wR of the refinements.

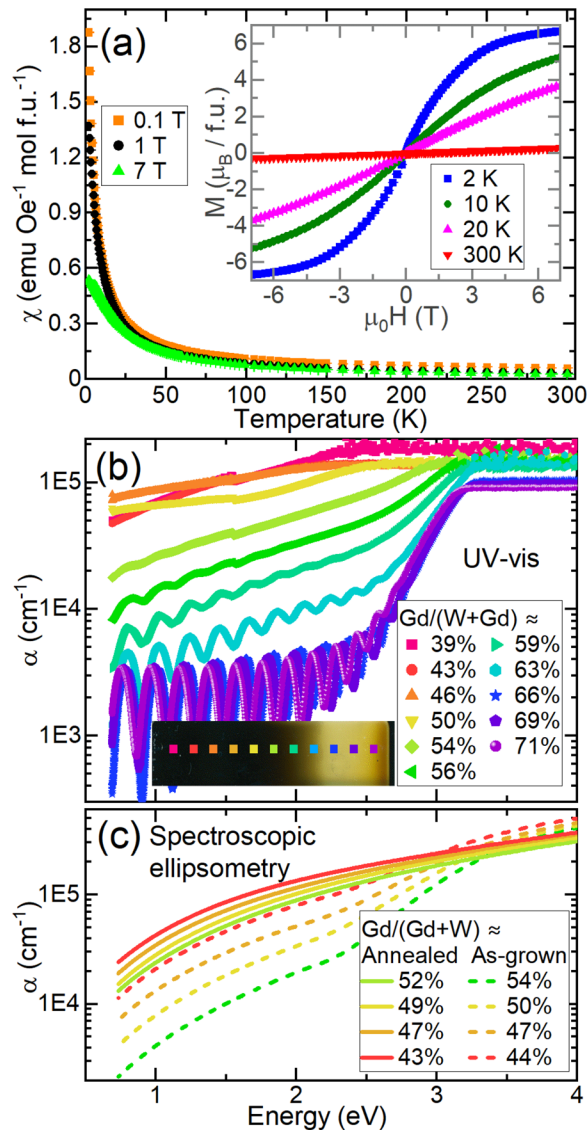
Space group	$a$ (Å)	$b$ (Å)	$c$ (Å)	Volume (Å <sup>3</sup> )	wR (%)
$Pnma$ (expt.)	5.636(1)	7.8214(5)	5.5252(4)	243.55(5)	1.68
$Pnma$ (calc.)	5.713	7.793	5.576	248.296	...
$Pnma$ (calc. error)	+1.4%	−0.4%	+0.9%	...	...
$R3c$ (expt.)	5.537(3)	...	13.567(6)	360.21(7)	2.16
$R3c$ (calc.)	5.610	...	13.812	376.478	...
$R3c$ (calc. error)	+1.3%	...	+1.8%	...	...
$Pm\bar{3}m$ (expt.)	3.916(2)	...	...	60.067(9)	2.16
$Pm\bar{3}m$ (calc.)	3.981	...	...	63.109	...
$Pm\bar{3}m$ (calc. error)	+1.7%	...	...	...	...

Our calculations predict an AFM ground state for  $Pnma$   $GdWN_3$  with the  $Gd^{3+}$  moments aligned along the  $c$  axis; they have parallel alignment within  $a$ - $c$  planes and anti-parallel alignment between adjacent  $a$ - $c$  planes stacked along the  $b$  axis [Fig. 3(c)]. This is similar to previous calculations of an AFM ground state with  $T_N > 2$  K for  $R3c$  and  $Pna2_1$  perovskite phases.<sup>17</sup> To test this experimentally, we performed temperature-dependent magnetic susceptibility measurements on a piece of a combinatorial film down to  $T = 2$  K, as shown in Fig. 4(a). The cation composition of this sample measured by XRF is  $Gd/(W + Gd) \approx 47\%$ . The diamagnetic contribution from the Si substrate was measured and subtracted, and the sample mass was calculated from the approximate film volume (see the [supplementary material](#) for details). The temperature-dependent susceptibility ( $\chi$ ) is consistent with paramagnetism down to  $T = 2$  K; there is no peak, and no splitting between zero-field-cooled and field-cooled data is observed at low applied field. The inset of Fig. 4(a) shows magnetization ( $M$ ) as a function of applied magnetic field at several temperatures. These data are also consistent with paramagnetism; no net moment is observed. We note that the oxygen-rich surface region observed in these films after air exposure may lead to some contribution from amorphous/nanocrystalline  $GdO_x$ , but as  $Gd_2O_3$  is PM, its presence does not change the overall conclusion.

A Curie-Weiss fit performed from 50 to 350 K on inverse susceptibility data collected with applied field  $\mu_0 H = 7$  T yields a Weiss

temperature of  $-4.7(1)$  K and an effective moment ( $\mu_{eff}$ ) of  $8.2(2) \mu_B$  per Gd (using a diamagnetic correction  $\chi_0 = 7.363 \times 10^{-4}$  emu/mol). This  $\mu_{eff}$  value is very close to the value expected for one isolated  $Gd^{3+}$  ( $8 \mu_B$ ), especially considering the many sources of potential error in quantifying the mass of the film. The slightly negative Weiss temperature indicates weak AFM correlations, consistent with previous and current theoretical predictions.<sup>17</sup> However, the data point to a lack of long-range order even at  $T = 2$  K. The calculated energy difference between PM and AFM states is  $0.838$  meV/f.u. (Table S2), consistent with weak AFM correlations. Despite the theoretical predictions of order,<sup>8,17</sup> the paramagnetism is not surprising given that the magnetic behavior of the only other reported nitride perovskites with a magnetic  $A$  cation— $CeMN_{3-y}$  with  $M = W, Mo$ —is somewhat similar.<sup>5</sup>  $CeWN_{3-y}$  is PM down to 2 K with a large, negative Weiss temperature indicating strong AFM correlations, and  $CeMoN_{3-y}$  is a frustrated AFM below  $T_N \approx 8$  K.<sup>5</sup> However, we note that the  $A = Ce$  case is much more complicated than the  $A = Gd$  case, as Ce, Mo, and W have multiple possible formal oxidation states, unlike Gd. The simpler  $GdWN_{3-y}$ , in which only the  $A$  site is magnetic, suggests that the low-temperature AFM order observed in  $CeMoN_{3-y}$  may be due to complex coupling between moments on both the  $A$ -site and  $B$ -site sublattices. Future strategies to induce long-range magnetic order in nitride perovskites may include increasing distortion in the perovskite lattice, as the  $Gd^{3+}$  cations are quite far from each other (nearly  $4 \text{ \AA}$ ) in the

**FIG. 3.** (a) Energies of  $GdWN_3$  polymorphic structures relative to the predicted ground-state  $Pnma$  structure.  $C2/c$  is not a perovskite phase, while the other structures are in the perovskite family. (b) Stable ground-state  $Pnma$  structure. (c) Antiferromagnetic ground-state structure of  $Pnma$   $GdWN_3$ .



**FIG. 4.** (a) Temperature-dependent magnetic susceptibility ( $\chi$ ) of  $\text{GdWN}_{3-y}$  at several applied fields. Inset: magnetization ( $M$ ) as a function of applied field. The measured film had  $\text{Gd}/(\text{W}+\text{Gd}) \approx 47\%$ . (b) and (c) Absorption coefficient ( $\alpha$ ) extracted from (b) UV-vis transmission spectroscopy and (c) spectroscopic ellipsometry measurements along compositionally graded  $\text{GdWN}_{3-y}$  films grown on sapphire for UV-vis and Si for SE. Inset of (b): a picture of the UV-vis film with the approximate measured locations marked. In (c), data from both as-grown and annealed (at 950 °C in flowing  $\text{N}_2$ ) films are shown.

structural models tested here, or designing materials with magnetic cations on both the A- and B-site sublattices.

Optical properties were probed with UV-vis transmission spectroscopy on an annealed film grown on a sapphire substrate, and the extracted absorption coefficients ( $\alpha$ ) are in Fig. 4(b). Across the wide composition gradient, there is a significant change in behavior: the most Gd-rich samples have an absorption onset of  $\sim 3$  eV. Fringes are visible in the data for Gd-rich regions, indicating uncorrected

reflections. We note that the measured film was approximately 700–1000 nm thick, with a thickness gradient corresponding to the composition gradient. As  $\text{Gd}/(\text{W} + \text{Gd})$  decreases, the absorption onset also decreases. Close to the point where the perovskite phase crystallizes, the fringes disappear and the behavior becomes highly absorbing across a wide energy range. GIWAXS data of the sample on which UV-vis was measured are in Fig. S6. The film is transparent yellow-brown in the Gd-rich region, above approximately  $\text{Gd}/(\text{W} + \text{Gd}) \approx 60\%$ . Below this, the film is dark, consistent with the higher absorption and possible metallic  $\text{W}/\text{WN}_x$  impurities. Additionally, spectroscopic ellipsometry data were collected on as-deposited and annealed perovskite films [Fig. 4(c)]. The as-deposited data were easily modeled as an amorphous semiconductor, while the annealed, crystalline samples were more difficult to model due to high optical absorption. The absorption increases upon annealing, particularly below  $\sim 3$  eV. The trends are consistent with those extracted from the UV-vis data at similar  $\text{Gd}/(\text{W} + \text{Gd})$  values.

We observe that the experimentally reported nitride perovskites are dominated by W as the B-site cation; only one example with  $B = \text{Mo}$ , which is directly above W in the periodic table and should thus follow similar trends, has been reported. Indeed, our attempts to synthesize  $\text{GdMoN}_3$  and  $\text{LaMoN}_3$  in a similar manner to  $\text{LaWN}_3$ ,<sup>1,14</sup>  $\text{CeWN}_3$ ,  $\text{CeMoN}_3$ ,<sup>5</sup> and now  $\text{GdWN}_3$  have been unsuccessful to date. We attempted RF co-sputtering with a range of experimental parameters (including varying the substrate temperature, deposition rate, activation of nitrogen via a nitrogen plasma cracker, biasing the substrate, and annealing *ex situ*) and did not observe the crystallization of a perovskite phase. This may be consistent with computational work predicting that the ground-state structure of  $\text{LaMoN}_3$  is not a perovskite and that pressure of  $\sim 1.5$  GPa is necessary to stabilize a perovskite phase.<sup>21</sup> However, similar calculations predicted analogous behavior for  $\text{GdWN}_3$ ,<sup>17</sup> which we show experimentally here does form a perovskite. The films resulting from our experimental attempts at  $\text{GdMoN}_3$  and  $\text{LaMoN}_3$  were generally highly air-sensitive and were often complex mixes of binary nitrides, oxides, and oxynitrides.  $\text{CeMoN}_{3-y}$  is the only Mo-containing nitride perovskite that has been successfully synthesized;<sup>5</sup> we hypothesize that it may be stabilized by the possibility of mixed  $\text{Ce}^{3+}/\text{Ce}^{4+}$  oxidation states compensated by  $\text{Mo}^{5+}/\text{Mo}^{6+}$ .

In conclusion, we present the synthesis and characterization of the first Gd-containing nitride perovskite,  $\text{GdWN}_{3-y}$ . Combinatorial RF co-sputtering with activated nitrogen yielded nanocrystalline films with a composition gradient. AES depth profiling and STEM-EDS elemental mapping reveal oxygen content  $y < 0.05$  in the bulk of the film, consistent with a primarily nitride compound. In contrast with previous ground-state structure calculations, an *ex situ* rapid thermal annealing step in flowing  $\text{N}_2$  crystallized a perovskite phase close to the  $\text{GdWN}_{3-y}$  composition. LeBail fits of synchrotron GIWAXS data are most consistent with the calculated ground-state *Pnma* perovskite structure. Density functional theory calculations reveal a perovskite ground state for  $\text{GdWN}_3$  in orthorhombic *Pnma* symmetry with AFM magnetic ordering of  $\text{Gd}^{3+}$ , in contrast to previous computational studies predicting a non-perovskite structure. Magnetic susceptibility reveals PM behavior down to 2 K with an effective moment of  $8.2(2) \mu_B$ , indicating isolated  $\text{Gd}^{3+}$  moments. The negative Weiss temperature suggests AFM correlations, consistent with calculations of an AFM ground state. Optical properties were studied across the

composition gradient, finding a higher absorption onset in Gd-rich samples and vice versa. Future work will be required to further explore and optimize this material. The high-throughput discovery and characterization of GdWN<sub>3-y</sub>, the first Gd-containing nitride perovskite, opens a pathway for understanding, designing, and controlling the properties of this emerging class of materials.

See the [supplementary material](#) for detailed experimental methods and additional AES, TEM, SEM, XRD, and calculation data, and the calculated crystallographic information file (CIF) for GdWN<sub>3</sub> in *Pnma* symmetry.

This work was authored by the National Renewable Energy Laboratory (NREL), operated by Alliance for Sustainable Energy, LLC, for the U.S. Department of Energy (DOE) under Contract No. DE-AC36-08GO28308. This work was supported by the Laboratory Directed Research and Development (LDRD) Program at NREL (R. W. Smaha, calculations). Funding was provided by the U.S. Department of Energy, Office of Science, Basic Energy Sciences, Division of Materials Science: through the Materials Chemistry program, as a part of the Early Career Award “Kinetic Synthesis of Metastable Nitrides” (development and operation of synthesis and characterization equipment); through the Funding Opportunity Announcement (FOA) No. DE-FOA-0002676: Chemical and Materials Sciences to Advance Clean-Energy Technologies and Transform Manufacturing (magnetic measurements), and through the Laboratory Program Announcement No. LAB 21-2491: Microelectronics Co-Design Research (microscopy, calculations). This work used computational resources sponsored by the Department of Energy’s Office of Energy Efficiency and Renewable Energy, located at NREL. Use of the Stanford Synchrotron Radiation Lightsource, SLAC National Accelerator Laboratory, is supported by the U.S. Department of Energy, Office of Science, Office of Basic Energy Sciences under Contract No. DE-AC02-76SF00515. The authors wish to thank the Analytical Resources Core (RRID: SCR\_021758) at Colorado State University for instrument access, training, and assistance with sample analysis. The authors thank N. Strange for support with GIWAXS measurements and P. Walker for assistance with the FIB liftout. The views expressed in the article do not necessarily represent the views of the DOE or the U.S. Government.

## AUTHOR DECLARATIONS

### Conflict of Interest

The authors have no conflicts to disclose.

### Author Contributions

**Rebecca W. Smaha:** Conceptualization (lead); Data curation (lead); Funding acquisition (lead); Investigation (lead); Project administration (lead); Writing – original draft (lead). **John S. Mangum:** Investigation

(equal); Writing – original draft (equal). **Neha Yadav:** Investigation (equal); Writing – review & editing (equal). **Christopher L. Rom:** Investigation (equal); Writing – review & editing (equal). **Brian M. Wieliczka:** Investigation (supporting). **Baptiste Julien:** Investigation (supporting). **Andrew Treglia:** Investigation (supporting). **Craig L. Perkins:** Investigation (supporting). **Prashun Gorai:** Data curation (equal); Writing – review & editing (equal). **Sage R. Bauers:** Methodology (equal); Supervision (equal); Writing – review & editing (equal). **Andriy Zakutayev:** Conceptualization (equal); Funding acquisition (equal); Methodology (equal); Resources (equal); Supervision (equal); Writing – review & editing (equal).

## DATA AVAILABILITY

The data that support the findings of this study are openly available at <https://hitem.nrel.gov>, Ref. 22.

## REFERENCES

- <sup>1</sup>K. R. Talley, C. L. Perkins, D. R. Diercks, G. L. Brennecke, and A. Zakutayev, *Science* **374**, 1488 (2021).
- <sup>2</sup>N. E. Brese and F. DiSalvo, *J. Solid State Chem.* **120**, 378 (1995).
- <sup>3</sup>S. Matsuishi, D. Iwasaki, and H. Hosono, *J. Solid State Chem.* **315**, 123508 (2022).
- <sup>4</sup>S. D. Kloß, M. L. Weidemann, and J. P. Attfield, *Angew. Chem., Int. Ed.* **60**, 22260 (2021).
- <sup>5</sup>R. Sherbondy, R. W. Smaha, C. J. Bartel, M. E. Holtz, K. R. Talley, B. Levy-Wendt, C. L. Perkins, S. Eley, A. Zakutayev, and G. L. Brennecke, *Chem. Mater.* **34**, 6883 (2022).
- <sup>6</sup>R. Sarmiento-Pérez, T. F. T. Cerqueira, S. Körbel, S. Botti, and M. A. L. Marques, *Chem. Mater.* **27**, 5957 (2015).
- <sup>7</sup>S. Körbel, M. A. Marques, and S. Botti, *J. Mater. Chem. C* **4**, 3157 (2016).
- <sup>8</sup>J. A. Flores-Livas, R. Sarmiento-Pérez, S. Botti, S. Goedecker, and M. A. L. Marques, *J. Phys. Mater.* **2**, 025003 (2019).
- <sup>9</sup>V-a Ha, H. Lee, and F. Giustino, *Chem. Mater.* **34**, 2107 (2022).
- <sup>10</sup>B. F. Grosso, D. W. Davies, B. Zhu, A. Walsh, and D. O. Scanlon, *Chem. Sci.* **14**, 9175 (2023).
- <sup>11</sup>A. Fuertes, *J. Mater. Chem.* **22**, 3293 (2012).
- <sup>12</sup>R. Niewa, *Eur. J. Inorg. Chem.* **32**, 3647 (2019).
- <sup>13</sup>K. Hanzawa and H. Hiramatsu, *ACS Appl. Electron. Mater.* **5**, 2793 (2023).
- <sup>14</sup>R. W. Smaha, J. S. Mangum, I. A. Leahy, J. Calder, M. P. Hautzinger, C. P. Muzzillo, C. L. Perkins, K. R. Talley, S. Eley, P. Gorai, S. R. Bauers, and A. Zakutayev, *Phys. Rev. Mater.* **7**, 084411 (2023).
- <sup>15</sup>M. Fiebig, T. Lottermoser, D. Meier, and M. Trassin, *Nat. Rev. Mater.* **1**, 16046 (2016).
- <sup>16</sup>N. A. Spaldin and R. Ramesh, *Nat. Mater.* **18**, 203 (2019).
- <sup>17</sup>C. Gui, J. Chen, and S. Dong, *Phys. Rev. B* **106**, 184418 (2022).
- <sup>18</sup>S. R. Bauers, A. Holder, W. Sun, C. L. Melamed, R. Woods-Robinson, J. Mangum, J. Perkins, W. Tumas, B. Gorman, A. Tamboli, G. Ceder, S. Lany, and A. Zakutayev, *Proc. Natl. Acad. Sci. U. S. A.* **116**, 14829 (2019).
- <sup>19</sup>S. Zhuk, A. A. Kistanov, S. C. Boehme, N. Ott, F. La Mattina, M. Stiefel, M. V. Kovalenko, and S. Siol, *Chem. Mater.* **33**, 9306 (2021).
- <sup>20</sup>A. L. Greenaway, S. Ke, T. Culman, K. R. Talley, J. S. Mangum, K. N. Heinselman, R. S. Kingsbury, R. W. Smaha, M. K. Gish, E. M. Miller, K. A. Persson, J. M. Gregoire, S. R. Bauers, J. B. Neaton, A. C. Tamboli, and A. Zakutayev, *J. Am. Chem. Soc.* **144**, 13673 (2022).
- <sup>21</sup>C. Gui and S. Dong, *Phys. Rev. B* **102**, 180103 (2020).
- <sup>22</sup>See <https://hitem.nrel.gov> for “National Renewable Energy Laboratory (NREL).”